1   **High-content assay for precision medicine discovery in cystic fibrosis.**

2   Stella Prins[1], Emily Langron[1], Cato Hastings[2], Emily J. Hill[1], Andra C. Stefan[3], Lewis D.

3   Griffin[2] and Paola Vergani[1]*

4

5   [1] Department of Neuroscience, Physiology and Pharmacology

6   [2] CoMPLEX

7   [3] Natural Sciences

8

9   University College London

10   Gower Street

11   WC1E 6BT London UK

12

13   The first two authors contributed equally to this project.

14   *Correspondence to: p.vergani@ucl.ac.uk

15

16   Keywords: CFTR, protein transport, ion channels, VX-770, fluorescence imaging.

Bullet point summary

What is already known:

- CFTR is an anion-selective channel, normally present in the plasma membrane of epithelial cells.

- Hundreds of different mutations affect CFTR biogenesis and/or function causing cystic fibrosis (CF).

What this study adds:

- We present and validate an assay that simultaneously measures CFTR biogenesis and function.

- Profiling a panel of CF-causing mutants suggests hypotheses on how approved drug VX-770 works.

Clinical Significance:

- The integrated assay boosts potential for discovery of more effective therapies, simultaneously repairing both defects.

Abstract

Background and Purpose: Cystic fibrosis (CF) is a life-limiting disease caused by mutations in the human *CFTR* gene, encoding an anion-selective channel. Because CF-causing mutations affect both CFTR permeation/gating and biogenesis, multi-assay approaches have been implemented in drug development, sequentially screening for channel function and membrane density. Here we present the first assay capable of simultaneous assessment of both CFTR characteristics.

Experimental approach: Images of live HEK293 cells co-expressing a soluble and a CFTR-tagged fluorescent protein are automatically acquired and analysed to quantify both CFTR membrane density and ion channel function. We monitor F508del-CFTR, the most common disease-causing mutant. Furthermore we characterize a panel of 62 CF-causing mutations and profile effects of acute treatment with approved drug VX-770, mapping potentiation on CFTR structures.

Key Results: We validate our assay by confirming F508del-CFTR rescue by incubation at low temperature, treatment with CFTR-targeting drugs and introduction of second-site revertant mutation R1070W. Measurements using the rare mutations panel also correlate well with published results.

49   *Conclusions and Implications:* Mapping of VX-770 potentiation of mutants suggests

50   that by increasing flexibility around the gate, the drug allows an alternative protein

51   conformation at domain interfaces around site 1.

52   The assay is a powerful tool for investigation of CFTR ion channel biophysics, allowing

53   more accurate inferences on gating/permeation properties than can be obtained by measuring

54   cellular conductance alone. Finally, by providing a two-dimensional molecular

55   characterization of individual mutant CFTR proteins, our assay can better inform development

56   of single-drug and combination therapies addressing the root cause of CF disease.

57

58 **Abbreviations**

59 ABC ATP-binding cassette

60 CF Cystic Fibrosis

61 CFTR Cystic Fibrosis Transmembrane Conductance Regulator

62 $F_{\text{YFP membrane}}$ average normalized YFP fluorescence intensity within the membrane zone

63 $F_{\text{mCherry cell}}$ average normalized mCherry fluorescence over the entire cell

64 G_{CFTR} CFTR conductance

65 G_{trans} transient anion conductance

66 IRES internal ribosome entry site

67 NBD nucleotide binding domain

68 PDL poly-D-lysine

69 P_{O} open probability

70 ρ CFTR membrane density

71 SSR sum of squared residuals

72 τ_{trans} time constant of the transient anion conductance

73 V_{M} membrane potential

74 WT wild type

75 YFP yellow fluorescent protein

4

Introduction

Cystic fibrosis (CF) is a life-limiting genetic disease most prevalent in people with a Caucasian background. Although the median survival age has increased by almost 12 years over the last decade, the disease strongly impacts expectation and quality of life (Elborn, 2016).

CF is caused by mutations in the *CFTR* gene (Riordan et al., 1989; Rommens et al., 1989), encoding an anion-selective channel (Csanády et al., 2019) present on the apical plasma membrane of epithelial cells. These mutations decrease the density of CFTR channels located on the cell membrane (by affecting protein synthesis, folding, intracellular trafficking, plasma membrane stability), and/or impair channel function (impacting on gating or anion permeation). As a result, transepithelial fluid movement is abnormal, creating problems particularly affecting lungs, pancreas, intestines, liver and reproductive systems.

Engineering of a halide sensitive YFP with increased affinity for iodide and a low affinity for chloride (Galietta et al., 2001a; Galietta et al., 2001b), allowed the first high throughput screening projects, which assessed CFTR activity by measuring the rate of YFP quenching caused by iodide influx and chloride efflux(Ma et al., 2002; Pedemonte et al., 2005a; Pedemonte et al., 2005b; Yang et al., 2003). Later, Vertex Pharmaceuticals used changes in membrane potential, monitored through fluorescence resonance energy transfer, to indirectly quantify CFTR channel function (Van Goor et al., 2009; Van Goor et al., 2006).

These efforts led to the identification of the first CFTR modulator drugs, directly targeting the defective CFTR protein. Modulators have been classified as either "potentiators", increasing CFTR channel function, or "correctors" increasing the number of CFTR channels on the plasma membrane. The potentiator ivacaftor (VX-770) (Van Goor et al., 2009) is now approved for the treatment of patients carrying the G551D gating mutation and a number of other mutations impairing channel function (Gentzsch & Mall, 2018). However, neither potentiation by VX-770 on its own (Flume et al., 2012), nor treatment with the corrector VX-809 (Van Goor et al., 2011) alone (Clancy et al., 2012), significantly improves lung function of patients homozygous for the F508del mutation, present on at least one allele in ~90% of patients. Like many other CF-causing mutations, F508del results not only in ion channel dysfunction, but also in a reduction of the number of channels present at the cell surface. Combination treatment with VX-770 and VX-809 provides small but significant health benefits (Wainwright et al., 2015). Triple combination therapies, combining two different correctors with a potentiator, hold promise to further improve patient outcomes (Davies et al., 2018; Keating et al., 2018).

109   More than 300 CF-causing mutations have been characterized (The Clinical and
110 Functional TRanslation of CFTR (CFTR2); available at http://cftr2.org). Each mutation, other
111 than F508del, is extremely rare, and is likely to affect the folding, trafficking, stability, gating
112 dynamics and/or permeation of the encoded CFTR protein differently. Pre-clinical data
113 informing on how drugs affect individual CFTR variants in simplified *in vitro* systems, is thus
114 very valuable for drug development and trial design.

115   Here we present a medium-throughput image-based assay that acquires multi-
116 dimensional data (dual-colour fluorescence intensity in time and space) on individual live
117 HEK293 cells and extracts information on two key characteristics of CFTR. By co-expressing
118 soluble mCherry with the halide sensitive YFP (Galietta et al., 2001a) linked to CFTR (Langron
119 et al., 2017), our new assay gives readouts of both CFTR function, and CFTR membrane
120 density. Experimental manipulation - incubation at low temperature (Denning et al., 1992;
121 Rennolds et al., 2008; Wang et al., 2008), treatment with VX-809 (He et al., 2013; Okiyoneda
122 et al., 2013) with and without VX-770 (Cholon et al., 2014; Veit et al., 2014), and addition of
123 revertant mutation R1070W (Farinha et al., 2013; Okiyoneda et al., 2013; Thibodeau et al.,
124 2010) - results in the expected changes in measured F508del-CFTR channel function and
125 membrane density. Furthermore, we present a screening platform suitable for profiling the
126 molecular characteristics of 62 CFTR variants carried by CF patients. Profiling the effects of
127 VX-770 (Vertex Pharmaceuticals) on this panel validates our new assay as a powerful tool for
128 "high-content" CFTR monitoring in pharmacological research.

129

130

131 **Results**

132 *The assay*

133   To obtain quantitative information about ion channel function of CFTR, we exploited
134 a halide-sensitive YFP (Galietta et al., 2001a; Galietta et al., 2001b), tagged to the N-terminal
135 of CFTR (Langron et al., 2018; Langron et al., 2017). We constructed a pIRES2-mCherry-
136 YFPCFTR plasmid that directs co-expression of YFP(H148Q/I152L)-CFTR (hereafter
137 designated YFP-WT-CFTR or simply WT-CFTR) and a soluble, cytosolic, red fluorescent
138 protein, mCherry (Shaner et al., 2004) (Figure 1A). The mCherry expression allows image
139 segmentation and localization of the cell membrane by marking the border of cells.
140 Furthermore, mCherry serves as an internal standard for the normalisation of YFP-CFTR
141 expression, eliminating variability due to unequal transfection efficiency.

142   Yellow fluorescence at the boundaries of areas of red fluorescence is used to estimate

143   CFTR membrane density for each cell (Figure 1). The "membrane" is defined as comprising a

144   ~1 μm wide band, on the inside of a cell's boundary. The density of CFTR at the membrane

145   (ρ), is estimated by dividing the average YFP-CFTR fluorescence intensity within the

146   membrane zone ($F_{\text{YFP membrane}}$), by the average mCherry fluorescence over the entire cell

147   ($F_{\text{mCherry cell}}$). The ρ metric can be thought of as the product of the proportion of CFTR localized

148   to the membrane ($F_{\text{YFP membrane}}/F_{\text{YFP cell}}$), multiplied by the metabolic stability of YFP-CFTR

149   with respect to mCherry ($F_{\text{YFP cell}}/F_{\text{mCherry cell}}$). Thus, changes in ρ metric will reflect not only

150   changes in CFTR trafficking, but also changes in the overall rates of biosynthesis vs.

151   degradation of the protein.

152

153   *Increasing F508del-CFTR membrane density*

154   To validate our assay, we assessed changes in F508del-CFTR membrane density by

155   comparing distributions of $\log_{10}\rho$ (logarithmic transformation of the ρ metric) obtained from

156   thousands of cells for each genotype/condition (Figure 2).

157

158   F508del-CFTR: VX-809 incubation

159   At 37°C, incubation with VX-809 for 24 hours caused a small but significant increase in $\log_{10}\rho$

160   of F508del-CFTR, (Figure 2A left, see also Supplementary Table S1). At 28°C, the magnitude

161   of the increase was greater (Figure 2A right).

162

163   F508del-CFTR: R1070W second-site revertant mutation

164   Introducing the second-site revertant mutation R1070W (Thibodeau et al., 2010) in the

165   F508del-CFTR background, significantly increased membrane density at 37°C, (Figure 2B left,

166   Supplementary Table S1), as well as at 28°C (Figure 2B right, Supplementary Table S1).

167   Again, the magnitude of the effect was larger at 28°C.

168

169   F508del-CFTR: chronic VX-770 incubation

170   When comparing cells expressing F508del-CFTR incubated for 24 hours with VX-809 alone,

171   with those incubated with both VX-809 and VX-770, at 37°C, there was a small but significant

172   decrease in $\log_{10}\rho$ (Figure 2C left, Supplementary Table S1). At 28°C the decrease was again

173   more pronounced than at 37°C (Figure 2C right).

174

175 F508del-CFTR: temperature correction

176 Because our fluorescence readings are normalized to those obtained from cells expressing WT-

177 CFTR grown on the same 96-well plate, we quantified the difference between the mean $\log_{10}\rho$

178 of WT-CFTR and F508del-CFTR at each temperature. The $\log_{10}\rho$ values of F508del-CFTR

179 were found to be significantly closer to those of WT-CFTR at 28°C, than at 37°C, (Figure 2D,

180 Supplementary Table S1).

181

182 *Increasing F508del-CFTR ion channel function*

183 Following addition of extracellular I^- (I^- first Protocol, see Methods), CFTR was

184 activated by 10 µM forskolin alone, or by a combination of 10 µM forskolin and 10 µM VX-

185 770 (the latter defined as an acute (a) treatment, as opposed to the 24-hour chronic (c)

186 incubation with VX-770 described above). The normalized fluorescence of HEK293-cells

187 expressing YFP-tagged WT-CFTR, F508del-CFTR, or F508del/R1070W-CFTRwas followed

188 over time (Figure 3). The maximal rate of I^- entry was used to summarize CFTR channel

189 function for the different CFTR genotypes, incubation and activation conditions tested (Figure

190 3E, Supplementary Tables S2 and S3). No significant difference in this metric was detected

191 among the different genotypes/conditions when DMSO (vehicle) was added instead of

192 activators .

193

194 WT-CFTR

195 As expected, in cells expressing WT-CFTR, the maximal rate of I^- entry was significantly

196 higher after activation with forskolin, compared to control (DMSO), at both 37°C and 28°C

197 (Figure 3A; Figure 3E WT). However, neither the presence of 10 µM VX-770 in addition to

198 forskolin during activation, nor incubation at 37°C vs. 28°C modified quenching rate

199 sufficiently to achieve statistical significance after multiple comparison correction (Figure 3A;

200 Figure 3E, WT, Supplementary Table S3).

201

202 F508del-CFTR: activation following temperature correction

203 Activation with forskolin alone failed to increase the maximal rate of I^- entry in untreated cells

204 expressing F508del-CFTR (Figure 3B top; Figure 3E F508del bars 1 and 4, Supplementary

205 Table S2), reflecting the severe gating defect which persists even after temperature correction.

206 Acute potentiation by VX-770 was required to detect function of the channels reaching the cell

207 surface thanks to temperature-correction (Figure 3B, bottom; Figure 3E F508del bars 5 vs. 2,

208 Supplementary Table S2).

209

210 <u>F508del-CFTR: activation following VX-809 correction</u>

211 At both temperatures, the activity of F508del-CFTR channels reaching the cell surface after

212 24-hour incubation with VX-809 could be detected following acute activation with forskolin

213 and VX-770. At 28°C the maximal rate of I⁻ entry was significantly greater than at 37°C (Figure

214 3C; Figure 3E, F508del bar 6 vs. 3, Supplementary Table S3).

215

216 <u>F508del-CFTR: rescue of ion channel function by the R1070W mutation</u>

217 Forskolin activation alone was enough to reveal F508del/R1070W-CFTR channel activity

218 (Figure 3D, Supplementary Table S2). The maximal rate of I⁻ entry was significantly higher at

219 28°C than at 37°C (Figure 3D; Figure 3E F508del/R1070W, Supplementary Table S3).

220

221 *The rare mutation panel*

222 CF-causing missense CFTR mutations (Sosnay et al., 2013; Van Goor et al., 2014; Yu

223 et al., 2012) were individually introduced in the pIRES2-mCherry-YFPCFTR plasmid, creating

224 a panel of 62 plasmids (including WT-CFTR as reference).

225 Following expression of the panel in HEK293 cells, and incubation with no

226 pharmacological correction, distributions for the ρ metric, and plate $\log_{10}\rho$ means were

227 obtained (Supplementary Table S4, Supplementary Figure S5). The data is summarized in

228 Figure 4A, which profiles membrane density for each CFTR mutant in the panel. Correlation

229 between our measured ρ and the proportion of CFTR acquiring complex glycosylation in FRT

230 cells is surprisingly good ($r^2 = 0.65$, Sosnay et al., 2013; $r^2 = 0.48$, Van Goor et al., 2014),

231 considering the differences in expression system and metric used (note that correlation between

232 the two published datasets is $r^2 = 0.48$).

233 YFP-CFTR fluorescence quenching experiments (I⁻ last Protocol, see Methods) were

234 carried out to estimate steady-state CFTR conductance (G_{CFTR}), without (DMSO) and with

235 baseline CFTR activation by 10 µM forskolin (Figure 4B-C; Supplementary Table S6). Again,

236 results correlate well with published data ($r^2 = 0.68$, Sosnay et al., 2013; $r^2 = 0.60$ Van Goor et

237 al., 2014). Conductance was also measured in the presence of 10 µM forskolin + 10 µM VX-

238 770 (Figure 4B, D; Supplementary Table S7). In these conditions, genotypes with high

9

239   conductance (including WT-CFTR) have faster YFP quenching than can be reliably measured

240   in our system. However, the assay can accurately monitor VX-770 potentiation when CFTR

241   activity is low, as is the case for most mutants (Van Goor et al., 2014).

Relationship between CFTR ion channel function and membrane density

243   By considering the changes in ion channel function in the context of any changes

244   measured in ρ, our assay allows more accurate inferences on the gating and permeation

245   properties of the CFTR channel molecules present at the cell surface.

246   Even when virtually no channels are present in the plasma membrane (as happens e.g.

247   for cells expressing F508del-CFTR incubated at 37^0 C) the value of ρ does not fall to zero.

248   This is likely due to some inaccuracy in automated cell boundary detection and to the widefield

249   microscope optics, resulting in stray light from out-of-focus planes reaching the

250   photomultiplier. To empirically investigate the relationship between G_{CFTR} and ρ, cells

251   expressing F508del-CFTR were treated with increasing concentrations of corrector VX-809,

252   progressively improving both biogenesis/membrane stability and conductance (Figure 5A).

253   Measured G_{CFTR} values as a function of ρ values show a roughly linear relationship. The

254   trendline can be extended to cross the ρ axis, extrapolating to an intercept at $\rho = 0.23$. In

255   addition, extension towards higher membrane densities shows how gating of F508del-CFTR,

256   VX-809-corrected and acutely potentiated by VX-770, reaches levels characteristic of WT-

257   CFTR (without potentiation), consistent with patch-clamp open probability (P_O) measurements

258   (Kopeikin et al., 2014; Wang et al., 2018).

259   Data on maximum rate of I⁻ entry can also be plotted against the corresponding ρ values,

260   measured for the different F508del-CFTR rescue strategies (Figure 5B). A linear interpolation

261   between data points for uncorrected F508del-CFTR and WT-CFTR activated by 10 μM

262   forskolin describes the ion channel function we would expect from cells with increasing CFTR

263   membrane density, assuming gating and permeation characteristics of baseline-activated WT-

264   CFTR. This allows us to infer how rescued F508del-CFTR channels reaching the membrane

265   compare to control channels in terms of function. The resulting x-axis intercept ($\rho = 0.25$) is

266   very similar to that obtained using G_{CFTR} to quantify ion channel function.

267   Introducing the R1070W revertant mutation in the F508del-CFTR background is shown

268   to be particularly effective in improving gating. Comparing revertant rescue with temperature

269   correction, Figure 5B shows how both strategies similarly increase membrane density but

270   temperature-corrected F508del-CFTR channels at the membrane have very low ion channel

271   function (unless acutely potentiated with VX-770). In contrast, F508del/R1070W channels at

272   the membrane have gating and permeation properties equal - or even superior - to WT-CFTR

273   (Figure 5B, cf. F508del/R1070W-CFTR red symbol vs. uncorrected F508del-CFTR blue

274   symbol). Both results are consistent with patch-clamp records indicating a F508del/R1070W-

275   CFTR P_O comparable to that of WT-CFTR (Liu et al., 2018), but a much lower P_O for

276   temperature-corrected F508del-CFTR (Kopeikin et al., 2014; Liu et al., 2018; Wang et al.,

277   2018) – note that single-channel conductance, γ, is unaffected by F508del and R1070W

278   mutations (Dalemans et al., 1991; Thibodeau et al., 2010).

279   Plots of G_{CFTR} as a function of ρ for the rare-mutation panel give an overview of

280   processing and gating/permeation defects caused by each missense mutation (Figure 5C). For

281   instance, D579G-CFTR (orange open diamond at coordinates (0.35,41.5)) falls close to the

282   WT-CFTR interpolation line, suggesting that the product of channel P_O and γ is not greatly

283   affected by this mutation, and that the low short-circuit currents measured in FRT cells (Sosnay

284   et al., 2013; Van Goor et al., 2014) are largely caused by the reduced membrane density. For

285   G1244E (orange (0.75,7.2)) and S549N (blue (0.83,11)), likely altering the structure of P- and

286   signature sequence loops, respectively, in site 2 measured ion channel function is much lower

287   than would be expected given the high membrane density. Here low short-circuit currents

288   (Sosnay et al., 2013) are likely due to gating defects. Most mutations give reduced membrane

289   densities and a conductance that falls below the interpolation line, suggesting processing

290   defects as well as some degree of impairment in gating/permeation for the molecules that do

291   reach the membrane. We further illustrate the effect of acute treatment with VX-770 for

292   mutations resulting in the strongest potentiation (fold-potentiation >20, Figure 5D). For many

293   of these, data points for potentiated conductance fall above the interpolation line, suggesting

294   that the product of P_O and γ is higher than measured for WT-CFTR in baseline-activated

295   conditions.

296

Discussion

298   Many CFTR variants associated with CF, including the most common, F508del-CFTR,

299   are characterized by both processing and functional defects. Rescue of either ion channel

300   function or membrane density alone, is not enough for effective treatment of patients (Clancy

301   et al., 2012; Flume et al., 2012). Therapies combining multiple correctors/potentiators are now

11

302   seen as most promising (Holguin, 2018). However, potentiators can negatively interfere with

303   corrector action (Cholon et al., 2014; Meng et al., 2017; Veit et al., 2014). Furthermore, it has

304   been suggested that maintaining a clear separation between correctors and potentiators does

305   not usefully describe CFTR pharmacology (Rowe & Verkman, 2013). Practical

306   implementation of distinct potentiator and corrector screens might have biased the search

307   towards combination therapies, hampering discovery of modulators with true dual activity. All

308   this highlights the potential impact of our assay, capable of simultaneously measuring

309   pharmacological effects on membrane localization and on gating/permeation characteristics.

310   Our assay accurately detects changes in membrane density of CFTR, even when such

311   changes are small and the heterogeneity among cells is large. Our assay can pick up a minute

312   difference in membrane density between untreated and VX-809 treated HEK293 cells

313   incubated at 37°C (Figure 2A left, Okiyoneda et al., 2013). The effect of the R1070W mutation

314   on F508del-CFTR membrane density at 37°C is similarly small (Okiyoneda et al., 2013, Figure

315   2B left). In agreement with other studies (Cholon et al., 2014; Veit et al., 2014), we observed

316   a small but significant shift in $\log_{10}\rho$ following chronic incubation with VX-770, consistent

317   with the potentiator destabilizing F508del-CFTR at the membrane (Figure 2C left). We were

318   also able to confirm that the membrane density of F508del-CFTR is increased at low

319   temperature (Denning et al., 1992; Rennolds et al., 2008; Wang et al., 2008, Figure 2D). The

320   effects of VX-809 treatment (He et al., 2013), R1070W rescue, and chronic treatment with VX-

321   770 on membrane density are larger when combined with incubation at low temperature

322   (Figure 2 right).

323   In addition to membrane density, our assay quantifies channel function,. Here, the assay

324   is not optimized to measure high CFTR activities and some measurements hit the upper limit

325   of its dynamic range (e.g. for WT-CFTR, Figs. 3 and 4, Supplementary Table S3). However,

326   both the "I⁻ first" protocol (Langron et al., 2017), measuring the maximal rate of I⁻ entry

327   ($\frac{\Delta[I^-]_{in}}{\Delta t}$) during CFTR activation, and "I⁻ last" protocol (Langron et al., 2018), estimating CFTR

328   conductance by fitting quenching time course after steady-state activation is reached, can

329   accurately quantify the low CFTR activities typically seen in mutants. While the "I⁻ last"

330   protocol is unaffected by variability in signal transduction kinetics and better accounts for

331   changing electrochemical potential gradients, the "I⁻ first" protocol allows faster data

332   acquisition and less computationally intensive analysis. In line with results obtained with other

333   techniques (e.g. Ussing chambers, high-throughput electrophysiology), our results show that

334 both G_{CFTR} (Sosnay et al., 2013; Van Goor et al., 2014) and $\frac{\Delta[I^-]_{in}}{\Delta t}$ (Billet et al., 2017; Van

335 Goor et al., 2011) provide accurate estimates of CFTR activity.

336   Accurate quantification of low conductance values is advantageous in characterizing

337 drug response by CFTR mutants, most of which have low residual activity. Our assay detects

338 strong VX-770 potentiation for R347P-, N1303K- and H1085R-CFTR, genotypes giving no

339 significant potentiation over baseline in the Ussing chamber study (Van Goor et al., 2014).

340 While further studies on the functional effects of R347P and H1085R mutations are required,

341 our results on N1303K are consistent with patch-clamp results (DeStefano et al., 2018). Such

342 mutants should not be described as not "responding" to VX-770, as it is likely that they might

343 benefit from therapies combining VX-770 with other modulators.

344   Empirical profiling of drug effects on the rare mutation panel can generate hypotheses

345 on drug mechanism of action. Considering the sites of mutations resulting in the highest VX-

346 770 efficacy (fold-potentiation >20, Figure 5D), these appear to link the ATP molecule bound

347 at site 1 to regions close to the narrowest portion of the permeation pathway, thought to

348 constitute the CFTR gate (El Hiani & Linsdell, 2010; Gao & Hwang, 2015), and positioned

349 adjacent to the very recently identified VX-770 binding site (Liu et al., 2019) (Figure 6). It is

350 interesting to note that ATP at site 1 contributes to stabilizing the opening transition state and

351 even more the prehydrolytic O_1 state (Sorum et al., 2017). Similarly, binding of VX-770 results

352 in an increased opening rate (Jih & Hwang, 2013) and a particularly stable O_1 state (Langron

353 et al., 2018).

354   Among the highly VX-770-sensitive mutations, all those surrounding the ATP and

355 NBD/TMD interface introduce charged side chains which would interact unfavourably with

356 other close charges in the conformation observed for phosphorylated, ATP-bound human

357 CFTR, carrying the open-state stabilizing E1371Q mutation, 6MSM (Zhang et al., 2018b): the

358 aspartate replacing G1349, in the NBD2 signature sequence, with the γ-phosphate bound at site

359 1 (Bompadre et al., 2007); the lysine in place of N1303 in the NBD2 "socket", with R1358 in

360 NBD2; the arginine replacing G178, in intracellular loop 1 (ICL1) with K254, E257 and R258

361 in ICL2 (Zhang et al., 2018b); the aspartate replacing H1054, in ICL4, with E543 in the NBD1

362 X-loop (He et al., 2008); the arginine in place of H1085, with R1048 in TM10 (for all listed

363 pairs distances between α-carbons are below 10 Å). Mutations at these sites are likely to

364 particularly destabilize the NBD-dimerized, ABC-canonical open channel conformation. It has

365 been recently suggested that "undocking" of NBD1 from the TMDs might occur

13

366   physiologically (Sigoillot et al., 2019). VX-770 binding might allow channels to reach an

367   alternative, particularly stable (Langron et al., 2018), open state, with a different conformation

368   at the interface between site 1 and the TMDs, possibly comprising an undocked NBD1.

369   Moreover, as the action of VX-770 has been found not to require ATP binding (Eckford et al.,

370   2012), with the increase in opening rate unaffected by [ATP] (Jih & Hwang, 2013), the stability

371   of this alternative open state (and of the transition state to reach it) might not be affected by

372   bound ATP molecules.

373   The remaining two highly VX-770-sensitive mutations insert prolines, known to restrict

374   backbone flexibility, in a region close to the CFTR gate. The R347P mutation, in TM6, affects

375   a residue important for maintaining a stable conducting pathway (Cotten & Welsh, 1999; Cui

376   et al., 2013; Kopeikin et al., 2010). The L927P mutation is in the unwound segment of TM8

377   (Corradi et al., 2018; Liu et al., 2017), underlying CFTR's unique channel function (Liu et al.,

378   2017). The very low conductance measured after baseline activation in both these mutants,

379   suggests that backbone flexibility at both these sites is required for channel opening and/or to

380   maintain a conducting permeation pathway (Zhang et al., 2018b). VX-770 has been

381   hypothesized to increase conformational flexibility of CFTR (Cholon et al., 2014) overall. It is

382   possible that this increased flexibility might particularly concern the extracellular end of

383   CFTR's transmembrane helices 8, 5, 4 and 6, surrounding the drug binding site, with VX-770

384   lubricating rearrangement of the helices and allowing adoption of the alternative open state

385   described above.

386   Acute treatment with VX-770 is most effective on L927P channels, resulting in an ~80-

387   fold potentiation. L927P is adjacent to A928, part of the VX-770 binding site (Liu et al., 2019).

388   However, patients carrying the L927P mutation are not currently among the genotypes

389   approved for VX-770 (alone or with corrector) treatment (Van Goor et al., 2014). Again, the

390   L927P CFTR genotype could well benefit from therapies combining VX-770 with other

391   modulators. Further investigation is required: patch-clamp recording of how the L927P-CFTR

392   ion channel function is altered by binding of VX-770, and studies on chronic rather than acute

393   treatment in native, patient-derived cells.

394   **Conclusions and Implications**

395   The main advantage of our assay consists in providing simultaneous measurements of

396   ion channel function and membrane density. Currently available high throughput assays report

397   on either CFTR membrane density or CFTR-mediated cellular conductance (G_{CFTR}). G_{CFTR} is

14

398 the product of 3 factors: the number of channels at the membrane (N), P_O, and γ ($G_{\text{CFTR}} = N \cdot$

399 $P_O \cdot \gamma$). Being able to monitor how compounds or mutations affect both number of channels at

400 the membrane and conductance can allow accurate deconvolution of effects on processing

401 (altering N) from those influencing gating and permeation of the channel (affecting P_O and γ,

402 respectively).

403 Describing each CF-causing mutation with two coordinates (ρ and G_{CFTR}) is a concise,

404 informative way of characterizing mutations (e.g. Figure 5C) and the effects of CFTR

405 modulators on them (e.g. Figure 5D). Implementing the assay at early stages (compound

406 screening and structure-activity relationship studies) could better inform drug development,

407 possibly enabling programmes seeking dual-activity (corrector/potentiator) modulators. In

408 addition, assay results obtained with our rare mutation panel could give valuable insight

409 relevant to patient stratification for clinical trial planning and/or could provide licensing

410 authorities with useful material on which to base decisions on regulatory approval for treatment

411 of patients with genotypes found only extremely rarely in the population (Ratner, 2017).

412 Finally, because CFTR plays an important role controlling fluid transport across several

413 epithelia (Frizzell & Hanrahan, 2012; Saint-Criq & Gray, 2017), it has been implicated in a

414 number of pathologies, including COPD (Solomon et al., 2017; Zhao et al., 2014), secretory

415 diarrhoeas (Thiagarajah et al., 2015), polycystic kidney disease (Li et al., 2012) and others

416 (Solymosi et al., 2013; Zhang et al., 2018a). It is likely that, given the complexity of CFTR

417 folding and trafficking (Farinha & Canato, 2017; Lukacs & Verkman, 2012), many CFTR-

418 targeting compounds will alter its cellular processing (Clunes et al., 2011), suggesting that the

419 assay could also be usefully deployed in the development of novel CFTR-targeting drugs for

420 other diseases, beyond CF.

Methods

Construction of the pIRES2-mCherry-YFPCFTR plasmid

The pIRES2-mCherry-YFPCFTR plasmid was obtained with two sequential subcloning steps. First, a 1.727kb region of pcDNA3.1-YFP-CFTR (Langron et al., 2017), containing the YFP-coding sequence, was subcloned into pIRES-eGFP-CFTR, a gift from David Gadsby (Rockefeller University), using the NheI and BlpI restriction sites. Subsequently a 0.737 kb region from pIRES2-mCherry-p53 deltaN (Lin et al., 2013) (Addgene), containing the mCherry-coding segment and part of the IRES, was subcloned into the pIRES-eGFP-YFPCFTR plasmid using the NotI and BmgBI/BtrI restriction sites. This resulted in the pIRES2-mCherry-YFPCFTR plasmid, with the IRES2 positioned between the two open reading frames for mCherry and YFP-CFTR.

HEK293 cell culture and transfection

HEK293 cells were maintained in Dulbecco's modified Eagle's medium (DMEM), supplemented with 2 mM L-glutamine, 100 U/mL penicillin and streptomycin, and 10% fetal bovine serum (all Life Technologies). Cells were seeded in poly-D-lysine-coated, black-walled 96-well plates (Costar, Fisher Scientific), and transiently transfected with the pIRES2-mCherry-YFPCFTR plasmid using Lipofectamine 2000 (Life Technologies). After transfection, cell plates were returned to the 37°C incubator for 24 hours. Prior to imaging plates were incubated for another 24 hours, at 37°C or 28°C, in 100 µL DMEM including DMSO (vehicle), 10 µM VX-809, or 10 µM VX-770 plus 10 µM VX-809 (Selleck Chemicals).

Image acquisition

Before imaging, cells were washed twice with 100 µL standard buffer (140 mM NaCl, 4.7 mM KCl, 1.2 mM MgCl2, 5 mM HEPES, 2.5 mM CaCl2, 1mM glucose, pH 7.4). The ImageXpress Micro XLS (Molecular Devices), an automated inverted wide-field fluorescence microscope with a temperature-controlled chamber (set to 37°C or 28°C, as indicated), was used for image acquisition. Protocols for automated fluid additions, enabled by a robotic arm, were created using MetaXpress software (Molecular Devices). For imaging of YFP(H148Q/I152L)-CFTR, a 472 ± 30 nm excitation filter, and a 520 ± 35 nm emission filter were used. Excitation/emission filters at 531 ± 20 nm and 592 ± 20 nm were used for imaging of mCherry.

453   For localization of CFTR, a 60× objective was used to take 9 16-bit images per well of

454   both fluorophores. To evaluate CFTR function, a 20× objective was used. Two 16-bit images

455   of mCherry were taken, one at the start and one the end of the protocol. In addition, 16-bit

456   images of the YFP fluorescence, were taken at an acquisition frequency of 0.5 Hz. For the I^-

457   first protocol ((A), see below), after 20 s, 50 µL of 300 mM I^- buffer (300 mM NaI, 4.7 mM

458   KCl, 1.2 mM $MgCl_2$, 5 mM HEPES, 2.5 mM $CaCl_2$,1mM glucose, pH 7.4) was added to the

459   standard buffer, so that the final concentration of I^- in the extracellular medium was 100 mM.

460   Another 40 s later, a further 50 µL of a 100 mM I^- buffer containing 40 µM forskolin (100 mM

461   NaI, 4.7 mM KCl, 1.2 mM $MgCl_2$, 5 mM HEPES, 2.5 mM $CaCl_2$,1mM glucose, 40 µM

462   forskolin, pH 7.4) was added, so that the final concentration of forskolin in the extracellular

463   medium was 10 µM, while concentration of I^- and other components remained unaltered. For

464   the I- last protocol ((B), below), after 20 s of imaging, CFTR was activated, in the absence of

465   extracellular iodide, by addition of 50 µl standard buffer containing activating compounds

466   (forskolin or forskolin + VX-770 both to reach final concentrations of 10 µM). After a further

467   230 s, by which time CFTR is assumed to be gating at steady state (Langron et al., 2018), 100

468   mM extracellular iodide (final concentration) was introduced by adding 50 µl of iodide buffer

469   (as standard buffer with 140 mM NaCl replaced with 400 mM NaI). Images were taken for 40

470   more seconds. Activating compounds were also included in the second addition so as not to

471   alter final extracellular concentrations.

472

473   *Image analysis*

474   Image analysis was automated using MATLAB mathematical computing software

475   (MathWorks). Separate analysis protocols were implemented to estimate CFTR membrane

476   density and ion channel function.

477

478   <u>CFTR membrane density</u>

479   First, mCherry images were binarized, and basic morphological operations (opening,

480   closing, area opening, and dilation) were carried out to reduce noise. A distance transform with

481   locally imposed minima was used to segment images by means of a watershed transformation

482   and define cell boundaries. Cells were removed from analysis if they had an area of under 108

483     $µm^2$ or over 5400 $µm^2$, if they had a major axis length of less than 32.4 µm, if the area over

484   perimeter was less than 25 or over 300, and if they were touching the edge of the image. A 1.08

485 μm band, 10 or 5 pixels wide (depending on the resolution of the image), within the border of

486 each cell was defined as the membrane zone.

487 Background was selected by inverting the binarized and morphologically opened

488 mCherry image, after which it was morphologically closed using a large structuring element to

489 prevent cells from being selected as background. Average background intensity was then

490 subtracted from each pixel, and the YFP and mCherry fluorescence intensity of each cell was

491 normalized to the median YFP and mCherry fluorescence intensities of cells expressing WT-

492 CFTR on the same plate. If the average normalized fluorescence intensity fell below 0 (due to

493 low transfection efficiency and high background noise), cells were removed from analysis.

494 In order to estimate CFTR membrane density for each cell (defined as ρ, see Results),

495 the average normalized YFP fluorescence intensity within the membrane zone was divided by

496 the average normalized mCherry fluorescence over the entire cell.

497
$$\rho = \frac{F_{\text{YFP membrane}}}{F_{\text{mCherry cell}}}$$

498

499 <u>CFTR ion channel function</u>

500 For assessment of CFTR function, two different protocols were used. For both, cells

501 were selected based on the mCherry fluorescence image that was taken at the beginning of the

502 protocol.

503 (A) I^- first Protocol

504 The fluorescence at the time point before addition of I^- was used to normalize YFP

505 fluorescence intensity. The concentration of I^- inside the cells ($[I^-]_{in}$) can be estimated with the

506 following equation (Langron et al., 2017), in which the binding affinity for I^- (K_I) to

507 YFP(H148Q/I152L) is 1.9 mM (Galietta et al., 2001a) and the normalized fluorescence

508 intensity over time ($F(t)$) is determined experimentally.

509
$$[I^-]_{in} = K_I \frac{(1 - F(t))}{F(t)}$$

510 Data is collected every 2 seconds, so the change $[I^-]_{in}$ observed at each time point can be

511 estimated and used to calculate the rate of I^- entry (in mM/s):

512
$$\frac{\Delta[I^-]_{in}}{\Delta t} = \frac{[I^-]_{in}(t) - [I^-]_{in}(t-1)}{2 \text{ s}}$$

513 The maximal observed rate of I^- entry is used as a measure of cellular anion conductance. To

514 determine whether there was increased CFTR-mediated anion conductance, the maximal rate

515 of I^- entry after addition of forskolin (which activates CFTR by cAMP dependent

18

516   phosphorylation), was compared to the maximal rate of I⁻ entry after addition of DMSO

517   (vehicle, negative control).

518   (B) I⁻ last Protocol

519   CFTR activation (by addition of 10 μM forskolin with or without 10 μM VX-770, as

520   indicated) was first allowed to reach steady state in the absence of I⁻ and quenching of YFP in

521   the 40 s following extracellular I⁻ addition was measured. A simple mathematical model was

522   used to fit observed fluorescence quenching, and estimate CFTR conductance as described

523   (Langron et al., 2018). Briefly, the model includes four free parameters: CFTR conductance at

524   steady-state (G_{CFTR}), membrane potential at steady-state, immediately prior to I⁻ addition (V_M),

525   and conductance (G_{trans}) and time constant (τ_{trans}) of a transient, endogenous non-CFTR anion

526   conductance. The values of the four parameters were estimated by minimizing the sum of

527   squared residuals obtained by comparing the time course of the observed average fluorescence

528   intensity within cells to the proportion of anion-free YFP chromophore predicted by the model

529   (both normalized to the time point before I⁻ addition). However, when the quenching time

530   course was too fast and did not provide enough information to uniquely identify all four

531   parameters, the value of the latter two parameters was constrained to the average values

532   obtained with negative controls, and only G_{CFTR} and V_M were estimated (Langron et al., 2018).

533   For both protocol (A) and (B) the value obtained from analysis of the observed YFP-

534   CFTR fluorescence quenching ($\frac{\Delta[I^-]_{in}}{\Delta t}$ and G_{CFTR}, respectively) was corrected for variations in

535   transfection efficiency, using the mean $F_{mCherry}$ within the cell selection normalized to $F_{mCherry}$

536   measured for WT in the same plate.

537

538   *Data and Statistical analysis*

539   The data and statistical analysis comply with the recommendations on experimental

540   design and analysis in pharmacology (Curtis et al., 2018). Measurements of conductance from

541   the rare mutation panel were repeated only on 3 or 4 independent samples (see Supplementary

542   Tables S6 and S7). As demonstrated by the good correlation with published datasets (see

543   Results) this is sufficient to give a first characterization of ion channel function, as is required

544   for most screens. No statistical analysis was performed on this dataset.

545   Because ρ values approach a log-normal distribution, values were log transformed

546   before performing statistical analysis, allowing parametric testing of the data. To determine

547   whether the observed differences in ρ, $\frac{\Delta[I^-]_{in}}{\Delta t}$, or G_{CFTR} resulting from experimental

548   manipulation and/or mutations were statistically significant, we performed either paired t-tests,

19

549   pairing conditions tested on the same plate, or independent t-tests. When required, either a

550   Bonferroni or a Benjamini-Hochberg correction was applied to adjust for multiple

551   comparisons. Data in graphs represent mean $\pm$ SEM, and the significance level was pre-

552   specified as $\alpha = 0.05$. Statistical analysis was carried out using MATLAB (MathWorks),

553   SigmaPlot (Systat Software), SPSS (IBM), or Excel (Microsoft).

554

Author Contributions

555

556   Experiments were conceived and designed by SP, EL and PV, after discussion with

557   LDG and CH. SP and EL, with the help of ACS, CH and EH, carried out the molecular biology,

558   ran the fluorescence assay acquisition and ran image analysis. SP, with the help of CH,

559   implemented the image analysis protocols and the mathematical model in the MATLAB

560   environment. Manuscript was written by SP, EL and PV. All authors read and commented on

561   the final draft of the manuscript.

Acknowledgements

562

Conflict of interest declaration

568

569   The authors declare no conflicts of interest.

References

Billet A, Froux L, Hanrahan JW, & Becq F (2017). Development of Automated Patch Clamp Technique to Investigate CFTR Chloride Channel Function. Front Pharmacol 8.

Bompadre SG, Sohma Y, Li M, & Hwang T-C (2007). G551D and G1349D, Two CF-associated Mutations in the Signature Sequences of CFTR, Exhibit Distinct Gating Defects. J Gen Physiol 129**:** 285-298.

Cholon DM, Quinney NL, Fulcher ML, Esther CR, Das J, Dokholyan NV*, et al.* (2014). Potentiator ivacaftor abrogates pharmacological correction of deltaF508 CFTR in cystic fibrosis. Sci Transl Med 6**:** 246ra296.

Clancy JP, Rowe SM, Accurso FJ, Aitken ML, Amin RS, Ashlock MA*, et al.* (2012). Results of a phase IIa study of VX-809, an investigational CFTR corrector compound, in subjects with cystic fibrosis homozygous for the F508del-CFTR mutation. Thorax 67**:** 12-18.

Clunes LA, Davies CM, Coakley RD, Aleksandrov AA, Henderson AG, Zeman KL*, et al.* (2011). Cigarette smoke exposure induces CFTR internalization and insolubility, leading to airway surface liquid dehydration. The FASEB Journal.

Corradi V, Gu R-X, Vergani P, & Tieleman DP (2018). Structure of Transmembrane Helix 8 and Possible Membrane Defects in CFTR. Biophys J 114**:** 1751-1754.

Cotten JF, & Welsh MJ (1999). Cystic Fibrosis-associated Mutations at Arginine 347 Alter the Pore Architecture of CFTR. Evidence for disruption of a salt bridge. J Biol Chem 274**:** 5429-5435.

Csanády L, Vergani P, & Gadsby DC (2019). STRUCTURE, GATING, AND REGULATION OF THE CFTR ANION CHANNEL. Physiol Rev 99**:** 707-738.

Cui G, Freeman CS, Knotts T, Prince CZ, Kuang C, & McCarty NA (2013). Two Salt Bridges Differentially Contribute to the Maintenance of Cystic Fibrosis Transmembrane Conductance Regulator (CFTR) Channel Function. J Biol Chem 288**:** 20758-20767.

Curtis MJ, Alexander S, Cirino G, Docherty JR, George CH, Giembycz MA*, et al.* (2018). Experimental design and analysis and their reporting II: updated and simplified guidance for authors and peer reviewers. Br J Pharmacol 175**:** 987-993.

Dalemans W, Barbry P, Champigny G, Jallat S, Jallat S, Dott K*, et al.* (1991). Altered chloride ion channel kinetics associated with the [Delta]F508 cystic fibrosis mutation. Nature 354**:** 526-528.

612   Davies JC, Moskowitz SM, Brown C, Horsley A, Mall MA, McKone EF, *et al.* (2018). VX-
613   659–Tezacaftor–Ivacaftor in Patients with Cystic Fibrosis and One or Two Phe508del Alleles.
614   N Engl J Med 379**:** 1599-1611.

615

616   Denning GM, Anderson MP, Amara JF, Marshall J, Smith AE, & Welsh MJ (1992). Processing
617   of mutant cystic fibrosis transmembrane conductance regulator is temperature-sensitive.
618   Nature 358**:** 761-764.

619

620   DeStefano S, Gees M, & Hwang T-C (2018). Physiological and pharmacological
621   characterization of the N1303K mutant CFTR. Journal of Cystic Fibrosis.

622

623   Eckford PDW, Li C, Ramjeesingh M, & Bear CE (2012). Cystic Fibrosis Transmembrane
624   Conductance Regulator (CFTR) Potentiator VX-770 (Ivacaftor) Opens the Defective Channel
625   Gate of Mutant CFTR in a Phosphorylation-dependent but ATP-independent Manner. J Biol
626   Chem 287**:** 36639-36649.

627

628   El Hiani Y, & Linsdell P (2010). Changes in Accessibility of Cytoplasmic Substances to the
629   Pore Associated with Activation of the Cystic Fibrosis Transmembrane Conductance Regulator
630   Chloride Channel. J Biol Chem 285**:** 32126-32140.

631

632   Elborn JS (2016). Cystic fibrosis. The Lancet 388**:** 2519-2531.

633

634   Farinha CM, & Canato S (2017). From the endoplasmic reticulum to the plasma membrane:
635   mechanisms of CFTR folding and trafficking. cell Mol Life Sci 74**:** 39-55.

636

637   Farinha CM, King-Underwood J, Sousa M, Correia Ana R, Henriques Barbara J, Roxo-Rosa
638   M, *et al.* (2013). Revertants, Low Temperature, and Correctors Reveal the Mechanism of
639   F508del-CFTR Rescue by VX-809 and Suggest Multiple Agents for Full Correction. Chem
640   Biol 20**:** 943-955.

641

642   Flume PA, Liou TG, Borowitz DS, Li H, Yen K, Ordoñez CL, *et al.* (2012). Ivacaftor in
643   subjects with cystic fibrosis who are homozygous for the f508del-cftr mutation. Chest 142**:**
644   718-724.

645

646   Frizzell RA, & Hanrahan JW (2012). Physiology of Epithelial Chloride and Fluid Secretion.
647   Cold Spring Harb Perspect Med 2.

648

649   Galietta L, Haggie P, & Verkman A (2001a). Green fluorescent protein-based halide indicators
650   with improved chloride and iodide affinities. FEBS Lett 499**:** 220-224.

651

652   Galietta L, Jayaraman S, & Verkman A (2001b). Cell-based assay for high-throughput
653   quantitative screening of CFTR chloride transport agonists. Am J Physiol Cell Physiol 281**:**
654   C1734-C1742.

655

656   Gao X, & Hwang T-C (2015). Localizing a gate in CFTR. Proceedings of the National
657   Academy of Sciences of the United States of America 112**:** 2461-2466.

658

659   Gentzsch M, & Mall MA (2018). Ion Channel Modulators in Cystic Fibrosis. Chest 154**:** 383-
660   393.

661

662   He L, Aleksandrov AA, Serohijos AWR, Hegedus T, Aleksandrov LA, Cui L*, et al.* (2008).
663   Multiple Membrane-Cytoplasmic Domain Contacts in the Cystic Fibrosis Transmembrane
664   Conductance Regulator (CFTR) Mediate Regulation of Channel Gating. J Biol Chem 283**:**
665   26383-26390.

666

667   He L, Kota P, Aleksandrov AA, Cui L, Jensen T, Dokholyan NV*, et al.* (2013). Correctors of
668   deltaF508 CFTR restore global conformational maturation without thermally stabilizing the
669   mutant protein. FASEB J 27**:** 536-545.

670

671   Holguin F (2018). Triple CFTR Modulator Therapy for Cystic Fibrosis. N Engl J Med 379**:**
672   1671-1672.

673

674   Jih K-Y, & Hwang T-C (2013). Vx-770 potentiates CFTR function by promoting decoupling
675   between the gating cycle and ATP hydrolysis cycle. Proceedings of the National Academy of
676   Sciences of the United States of America 110**:** 4404-4409.

677

678   Keating D, Marigowda G, Burr L, Daines C, Mall MA, McKone EF*, et al.* (2018). VX-445–
679   Tezacaftor–Ivacaftor in Patients with Cystic Fibrosis and One or Two Phe508del Alleles. New
680   England Journal of Medicine 379**:** 1612-1620.

681

682   Kopeikin Z, Sohma Y, Li M, & Hwang T-C (2010). On the mechanism of CFTR inhibition by
683   a thiazolidinone derivative. J Gen Physiol 136**:** 659.

684

685   Kopeikin Z, Yuksek Z, Yang HY, & Bompadre SG (2014). Combined effects of VX-770 and
686   VX-809 on several functional abnormalities of F508del-CFTR channels. Journal of Cystic
687   Fibrosis 13**:** 508-514.

688

689   Langron E, Prins S, & Vergani P (2018). Potentiation of the cystic fibrosis transmembrane
690   conductance regulator by VX-770 involves stabilization of the pre-hydrolytic, O1 state. Br J
691   Pharmacol 175**:** 3990-4002.

692

693   Langron E, Simone MI, Delalande CMS, Reymond J-L, Selwood DL, & Vergani P (2017).
694   Improved fluorescence assays to measure the defects associated with F508del-CFTR allow
695   identification of new active compounds. Br J Pharmacol 174**:** 525-539.

696

697   Li H, Yang W, Mendes F, Amaral MD, & Sheppard DN (2012). Impact of the cystic fibrosis
698   mutation F508del-CFTR on renal cyst formation and growth. Am J Physiol Renal Physiol 303**:**
699   F1176-F1186.

701   Lin S-C, Karoly ED, & Taatjes DJ (2013). The human ΔNp53 isoform triggers metabolic and
702   gene expression changes that activate mTOR and alter mitochondrial function. Aging Cell 12**:**
703   863-872.

705   Liu F, Zhang Z, Csanády L, Gadsby DC, & Chen J (2017). Molecular Structure of the Human
706   CFTR Ion Channel. Cell 169**:** 85-95.e88.

708   Liu F, Zhang Z, Levit A, Levring J, Touhara KK, Shoichet BK*, et al.* (2019). Structural
709   identification of a hotspot on CFTR for potentiation. Science 364**:** 1184-1188.

711   Liu J, Bihler H, Farinha CM, Awatade NT, Romão AM, Mercadante D*, et al.* (2018). Partial
712   rescue of F508del-cystic fibrosis transmembrane conductance regulator channel gating with
713   modest improvement of protein processing, but not stability, by a dual-acting small molecule.
714   Br J Pharmacol 175**:** 1017-1038.

716   Lukacs GL, & Verkman AS (2012). CFTR: folding, misfolding and correcting the [delta]F508
717   conformational defect. Trends Mol Med 18**:** 81-91.

719   Ma T, Vetrivel L, Yang H, Pedemonte N, Zegarra-Moran O, Galietta LJV*, et al.* (2002). High-
720   affinity Activators of Cystic Fibrosis Transmembrane Conductance Regulator (CFTR)
721   Chloride Conductance Identified by High-throughput Screening. J Biol Chem 277**:** 37235-
722   37241.

724   Meng X, Wang Y, Wang X, Wrennall JA, Rimington TL, Li H*, et al.* (2017). Two Small
725   Molecules Restore Stability to a Subpopulation of the Cystic Fibrosis Transmembrane
726   Conductance Regulator with the Predominant Disease-causing Mutation. J Biol Chem 292**:**
727   3706-3719.

729   Okiyoneda T, Veit G, Dekkers JF, Bagdany M, Soya N, Xu H*, et al.* (2013). Mechanism-based
730   corrector combination restores deltaF508-CFTR folding and function. Nat Chem Biol 9**:** 444-
731   454.

733   Pedemonte N, Lukacs GL, Du K, Caci E, Zegarra-Moran O, Galietta LJV*, et al.* (2005a). Small-
734   molecule correctors of defective {Delta}F508-CFTR cellular processing identified by high-
735   throughput screening. J Clin Invest 115**:** 2564-2571.

737   Pedemonte N, Sonawane ND, Taddei A, Hu J, Zegarra-Moran O, Suen YF*, et al.* (2005b).
738   Phenylglycine and Sulfonamide Correctors of Defective {Delta}F508 and G551D Cystic
739   Fibrosis Transmembrane Conductance Regulator Chloride-Channel Gating. Mol Pharmacol
740   67**:** 1797-1807.

741

742 Ratner M (2017). FDA deems in vitro data on mutations sufficient to expand cystic fibrosis
743 drug label. Nature Biotechnology 35**:** 606.

744

745 Rennolds J, Boyaka PN, Bellis SL, & Cormet-Boyaka E (2008). Low temperature induces the
746 delivery of mature and immature CFTR to the plasma membrane. Biochem Biophys Res
747 Commun 366**:** 1025-1029.

748

749 Riordan JR, Rommens JM, Kerem B, Alon N, Rozmahel R, Grzelczak Z*, et al.* (1989).
750 Identification of the cystic fibrosis gene: cloning and characterization of complementary DNA.
751 Science 245**:** 1066-1073.

752

753 Rommens JM, Iannuzzi MC, Kerem B-s, Drumm ML, Melmer G, Dean M*, et al.* (1989).
754 Identification of the Cystic Fibrosis Gene: Chromosome Walking and Jumping. Science 245**:**
755 1059-1065.

756

757 Rowe SM, & Verkman AS (2013). Cystic Fibrosis Transmembrane Regulator Correctors and
758 Potentiators. Cold Spring Harb Perspect Med 3**:** a009761.

759

760 Saint-Criq V, & Gray MA (2017). Role of CFTR in epithelial physiology. Cellular and
761 Molecular Life Sciences 74**:** 93-115.

762

763 Shaner NC, Campbell RE, Steinbach PA, Giepmans BNG, Palmer AE, & Tsien RY (2004).
764 Improved monomeric red, orange and yellow fluorescent proteins derived from Discosoma sp.
765 red fluorescent protein. Nat Biotechnol 22**:** 1567.

766

767 Sigoillot M, Overtus M, Grodecka M, Scholl D, Garcia-Pino A, Laeremans T*, et al.* (2019).
768 Domain-interface dynamics of CFTR revealed by stabilizing nanobodies. Nature
769 Communications 10**:** 2636.

770

771 Solomon GM, Fu L, Rowe SM, & Collawn JF (2017). The therapeutic potential of CFTR
772 modulators for COPD and other airway diseases. Current Opinion in Pharmacology 34**:** 132-
773 139.

774

775 Solymosi EA, Kaestle-Gembardt SM, Vadász I, Wang L, Neye N, Chupin CJA*, et al.* (2013).
776 Chloride transport-driven alveolar fluid secretion is a major contributor to cardiogenic lung
777 edema. Proceedings of the National Academy of Sciences of the United States of America 110**:**
778 E2308-E2316.

779

780 Sorum B, Töröcsik B, & Csanády L (2017). Asymmetry of movements in CFTR's two ATP
781 sites during pore opening serves their distinct functions. eLife 6**:** e29013.

782

783   Sosnay PR, Siklosi KR, Van Goor F, Kaniecki K, Yu H, Sharma N, *et al.* (2013). Defining the
784   disease liability of variants in the cystic fibrosis transmembrane conductance regulator gene.
785   Nat Genet 45**:** 1160-1167.

786
787   Thiagarajah JR, Donowitz M, & Verkman AS (2015). Secretory diarrhoea: mechanisms and
788   emerging therapies. Nat Rev Gastroenterol Hepatol 12**:** 446-457.

789
790   Thibodeau PH, Richardson JM, Wang W, Millen L, Watson J, Mendoza JL, *et al.* (2010). The
791   Cystic Fibrosis-causing Mutation deltaF508 Affects Multiple Steps in Cystic Fibrosis
792   Transmembrane Conductance Regulator Biogenesis. J Biol Chem 285**:** 35825-35835.

793
794   Van Goor F, Hadida S, Grootenhuis PDJ, Burton B, Cao D, Neuberger T, *et al.* (2009). Rescue
795   of CF airway epithelial cell function in vitro by a CFTR potentiator, VX-770. Proceedings of
796   the National Academy of Sciences of the United States of America 106**:** 18825-18830.

797
798   Van Goor F, Hadida S, Grootenhuis PDJ, Burton B, Stack JH, Straley KS, *et al.* (2011).
799   Correction of the F508del-CFTR protein processing defect in vitro by the investigational drug
800   VX-809. Proceedings of the National Academy of Sciences of the United States of America
801   108**:** 18843-18848.

802
803   Van Goor F, Straley KS, Cao D, Gonzalez J, Hadida S, Hazlewood A, *et al.* (2006). Rescue of
804   {Delta}F508-CFTR trafficking and gating in human cystic fibrosis airway primary cultures by
805   small molecules. Am J Physiol Lung Cell Mol Physiol 290**:** L1117-1130.

806
807   Van Goor F, Yu H, Burton B, & Hoffman BJ (2014). Effect of ivacaftor on CFTR forms with
808   missense mutations associated with defects in protein processing or function. J Cyst Fibros 13**:**
809   29-36.

810
811   Veit G, Avramescu RG, Perdomo D, Phuan P-W, Bagdany M, Apaja PM, *et al.* (2014). Some
812   gating potentiators, including VX-770, diminish F508del-CFTR functional expression. Sci
813   Transl Med 6**:** 246ra297.

814
815   Wainwright CE, Elborn JS, Ramsey BW, Marigowda G, Huang X, Cipolli M, *et al.* (2015).
816   Lumacaftor−Ivacaftor in Patients with Cystic Fibrosis Homozygous for Phe508del CFTR. N
817   Engl J Med 373**:** 220-231.

818
819   Wang X, Koulov AV, Kellner WA, Riordan JR, & Balch WE (2008). Chemical and Biological
820   Folding Contribute to Temperature-Sensitive ΔF508 CFTR Trafficking. Traffic 9**:** 1878-1893.

821
822   Wang Y, Cai Z, Gosling M, & Sheppard DN (2018). Potentiation of the cystic fibrosis
823   transmembrane conductance regulator Cl− channel by ivacaftor is temperature independent.
824   American Journal of Physiology-Lung Cellular and Molecular Physiology 315**:** L846-L857.

825

826   Yang H, Shelat AA, Guy RK, Gopinath VS, Ma T, Du K, *et al.* (2003). Nanomolar Affinity
827   Small Molecule Correctors of Defective {Delta}F508-CFTR Chloride Channel Gating. J Biol
828   Chem 278**:** 35079-35085.

829

830   Yu H, Burton B, Huang C-J, Worley J, Cao D, Johnson Jr JP, *et al.* (2012). Ivacaftor
831   potentiation of multiple CFTR channels with gating mutations. J Cyst Fibros 11**:** 237-245.

832

833   Zhang J, Wang Y, Jiang X, & Chan HC (2018a). Cystic fibrosis transmembrane conductance
834   regulator—emerging regulator of cancer. Cellular and Molecular Life Sciences 75**:** 1737-1756.

835

836   Zhang Z, Liu F, & Chen J (2018b). Molecular structure of the ATP-bound, phosphorylated
837   human CFTR. Proceedings of the National Academy of Sciences of the United States of
838   America.

839

840   Zhao R, Liang X, Zhao M, Liu S-L, Huang Y, Idell S, *et al.* (2014). Correlation of Apical
841   Fluid-Regulating Channel Proteins with Lung Function in Human COPD Lungs. PLOS ONE
842   9**:** e109725.

843

844

845

Figures and figure legends

Figure 1
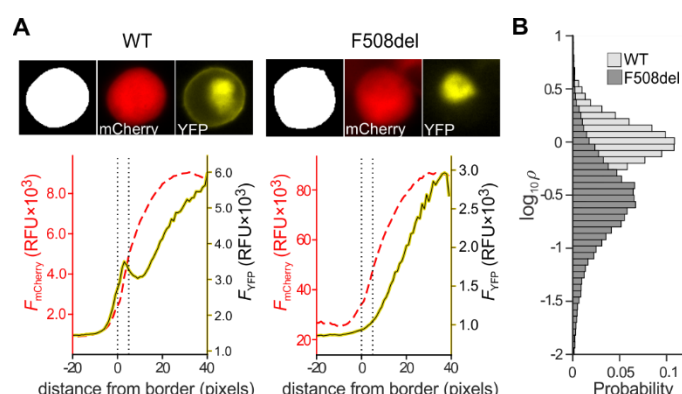
Image analysis to quantify CFTR membrane density (**A**) Image analysis of individual representative HEK293 cells transfected with pIRES2-mCherry-YFP-WT-CFTR (left), and pIRES2-mCherry-YFP-F508del-CFTR (right). Upper panels: boundary delimiting cell (white) from non-cell (black) is obtained from mCherry image (centre). CFTR cellular localization is obtained from YFP image (right). Lower panels: average mCherry fluorescence intensity (F_{mCherry}, red dashed line), and average YFP fluorescence intensity (F_{YFP}, solid yellow line), as a function of the distance from cell border. Membrane density is defined as

$$\rho = \frac{F_{\mathrm{YFP\ membrane}}}{F_{\mathrm{mCherry\ cell}}}$$

where $F_{\mathrm{YFP\ membrane}}$ is the average fluorescence intensity within the 'membrane' zone, set between 0 and 5 pixels from the cell border. (**B**) Probability density distribution of $\log_{10}\rho$ for cells expressing YFP-WT-CFTR (light grey), and YFP-F508del-CFTR (dark grey), incubated at 37 °C. For the WT cell shown, $\rho = 1.60$; for the F508del cell, $\rho = 0.25$.

28

Figure 2
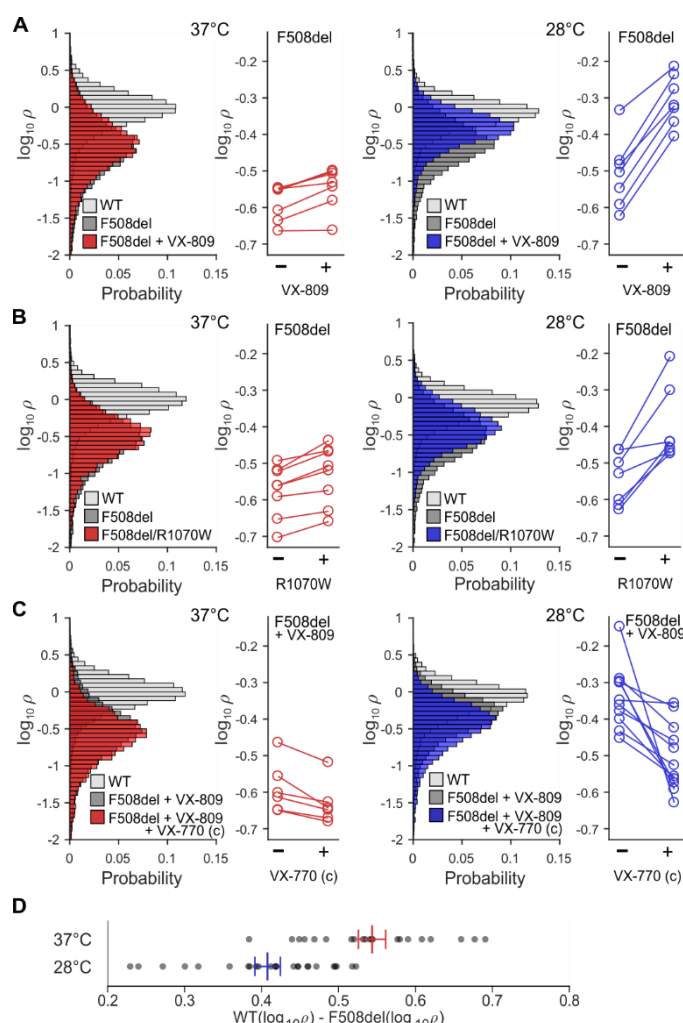
Monitoring CFTR membrane density ($\log_{10}\rho$) in HEK293 cells expressing WT-CFTR, F508del-CFTR, or F508del/R1070W-CFTR. Effects of chronic treatment with 10 µM VX-809 (**A**), R1070W rescue (**B**), and chronic treatment with 10 µM VX-809 + 10 µM VX-770 (**C**), on $\log_{10}\rho$ at 37°C (left, red) and 28°C (right, blue). Conditions of final incubation were maintained during image acquisition. The probability distributions in the panels on the left, contain $\log_{10}\rho$ measurements from thousands of cells, pooled from all experiments. For statistical analysis, mean $\log_{10}\rho$ values determined in independent experiments, and paired per plate, were used (displayed in panels on the right) (**D**) Before imaging, plates were incubated at 37°C, or 28°C for 24 hours. For each plate, the difference between mean $\log_{10}\rho$ for WT-CFTR and F508del-CFTR was calculated (WT($\log_{10}\rho$) - F508del($\log_{10}\rho$), grey dots). Red (37°C) and blue (28°C) lines show mean ± SEM, calculated from 21(37°C) and 25(28°C) within-plate difference estimates.

29

Figure 3
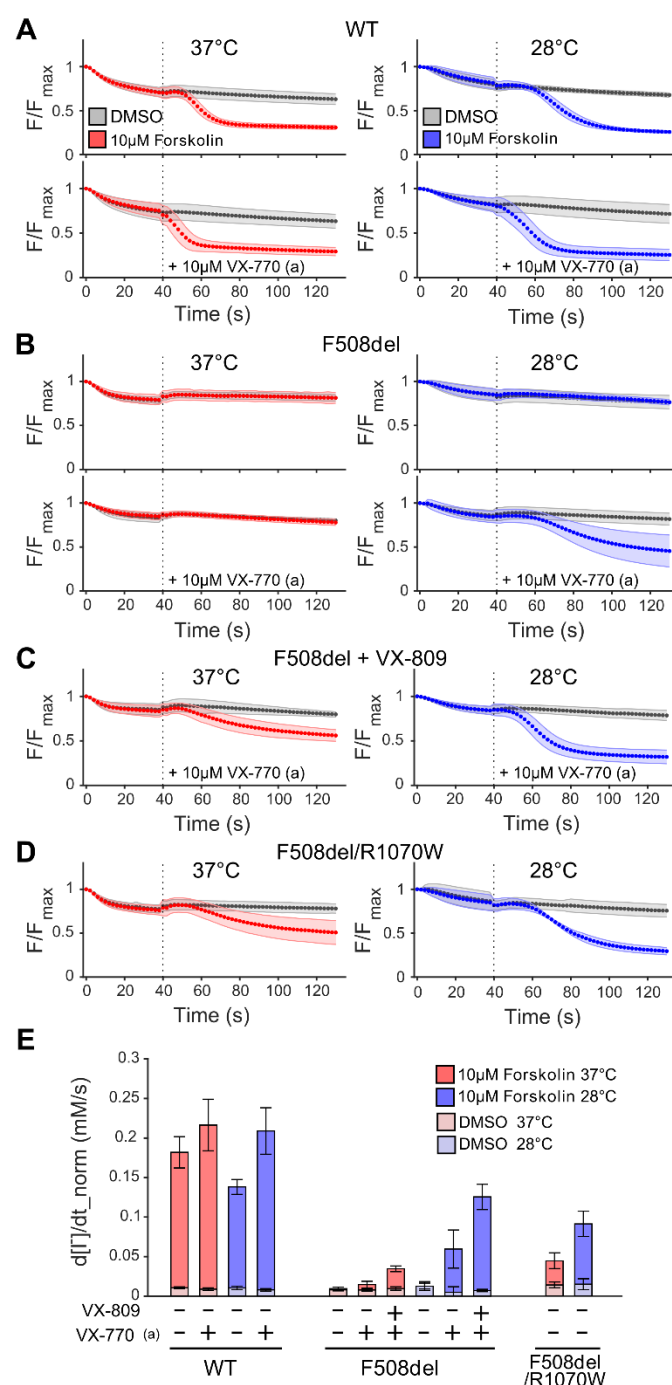
Monitoring CFTR ion channel function. (**A-D**) Quenching of YFP fluorescence in HEK293 cells expressing WT-CFTR (**A**), F508del-CFTR chronically (24 h) treated with DMSO (**B**) or with VX-809 (**C**), and R1070W/F508del-CFTR (**D**). For more information on statistical analysis see Supplementary Tables S2 and S3. Prior to imaging plates were incubated for 24 hours, at 37°C (left panels, red) or 28°C (right panels, blue). This final incubation temperature was maintained throughout image acquisition. At time point 0 s I⁻ was added to the extracellular medium. At 40 s forskolin and, where indicated, VX-770 (acute, a) was added (dotted line),

887   both to a final concentration of 10 µM. The fluorescence before addition of I⁻ (F_{max}), was used

888   to normalize YFP fluorescence intensity. (**E**) The maximal rate of I⁻ entry (d[I⁻]/dt_norm) is

889   used to summarize CFTR function for genotypes and conditions shown in (**A**-**D**).

890 **Figure 4**
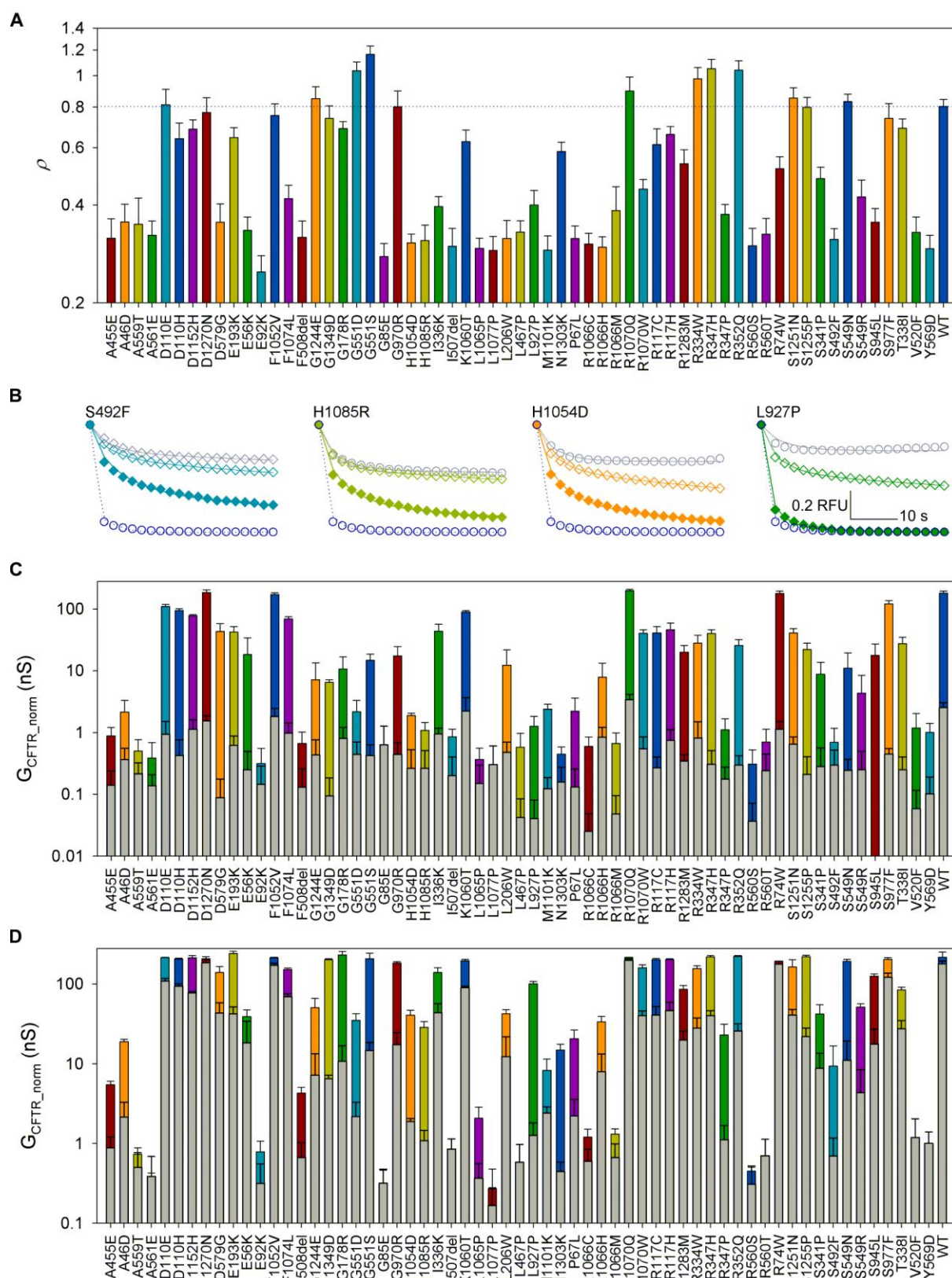
891   Rare CF-mutation profiling. (**A**) Mean ρ (n $\geq$ 9) of all mutations in the panel. Dotted line

892   indicates mean ρ for WT-CFTR. For ρ distributions, mean ρ and n values for each mutant see

893   Supplementary Figure S5 and Supplementary Table S4. (**B**) Observed YFP quenching time

894   course in the presence of DMSO (grey circles) or 10 µM forskolin (empty coloured diamonds),

895   or 10 µM forskolin + acute 10 µM VX-770 (filled coloured diamonds) for selected mutations.

896   Solid lines show predicted change in proportion of anion-free YFP. For estimated parameters

897   G_{CFTR}, V_M, G_{trans} and τ_{trans} see Supplementary Table S8. WT-CFTR quenching in 10 µM

898   forskolin (dark blue empty circles and dotted line) shown for comparison. (**C**) CFTR

899   conductance of rare mutation panel after activation with 10 µM forskolin (coloured bars) or

900   vehicle control (DMSO, grey bars). n $\geq$ 3. G_{CFTR} obtained from fitting of quenching time-course

901   for each mutant was normalized using the mean within cell mCherry fluorescence for that

902   mutant, measured with respect to the corresponding metric obtained for WT-CFTR on the same

903   plate. (**D**) Potentiation of rare mutation panel by VX-770. Grey bars show values following

904   activation with 10 µM forskolin alone, coloured bars with further addition of acute 10 µM VX-

905   770. For more information on statistical analysis of quenching data see Supplementary Tables

906   S6 and S7.

Figure 5
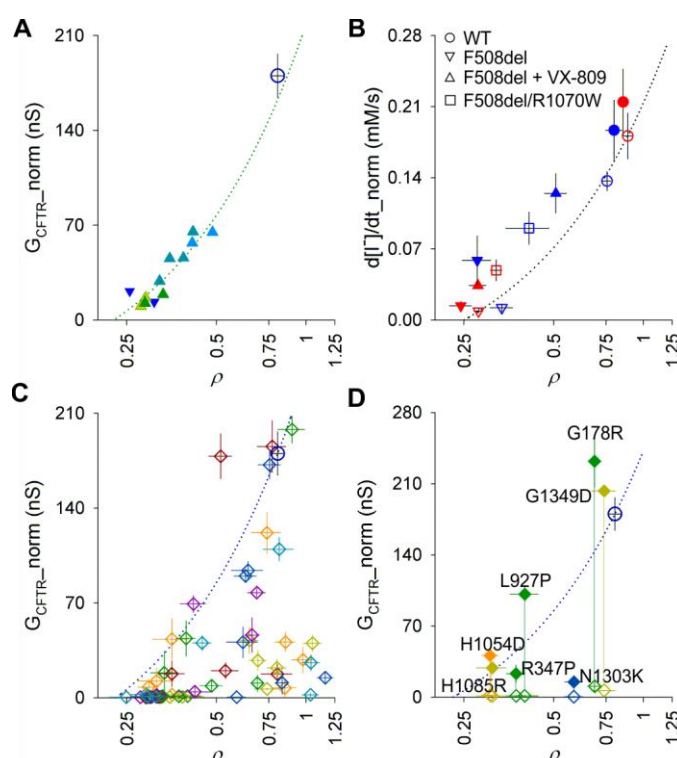
Investigating permeation/gating characteristics. (**A**) Relationship between normalized CFTR conductance and membrane density in cells expressing F508del-CFTR with no correction (blue ∇) or incubated with increasing concentrations of VX-809 (1 nM to 10 μM, green to light blue Δ), all after activation with 10 μM forskolin and acute potentiation with 10 μM VX-770. F508del-CFTR incubation and measurements were at 28°C. Green dotted line shows linear regression using only F508del-CFTR data points on graph (slope = 281.7, constant = -63.7, resulting in an x-axis intercept at $\rho = 0.23$). Mean value for WT-CFTR activated with 10 μM forskolin alone is shown for reference (from (**C**), large dark blue empty circle). (**B**) Relationship between maximal rate of I⁻ influx and ρ in HEK293 cells expressing WT-CFTR, F508del-CFTR, and F508del/R1070W-CFTR, at 37°C (red) and 28°C (blue). 10 μM forskolin was used to activate CFTR. Empty symbols indicate activation with forskolin alone. Solid symbols indicate further acute potentiation with 10 μM VX-770. Dotted line: linear interpolation between data obtained at 37°C for uncorrected F508del-CFTR and WT-CFTR, both without acute VX-770 potentiation; slope = 0.284, constant = -0.071, resulting in an x-axis intercept at $\rho = 0.25$. (**C**) Relationship between baseline G_{CFTR_norm} (10 μM forskolin) and ρ for rare mutation panel. Colours as in Figure 4. WT-CFTR is highlighted as a large, dark blue, empty circle. The dark blue dotted line (slope = 314.1, constant= -72.3) shows linear

34

926   interpolation between WT data points and x-axis intercept set at ρ =0.23, as obtained in (**A**).

927   (**D**) Mutants with largest fold potentiation by VX-770 (ratio between conductance obtained in

928   10 μM forskolin + 10 μM VX-770 over that in 10 μM forskolin alone > 20). Empty diamonds

929   indicate baseline activation with 10 μM forskolin alone, solid diamonds indicate activation

930   following acute potentiation with 10 μM forskolin + 10 μM VX-770.

Figure 6
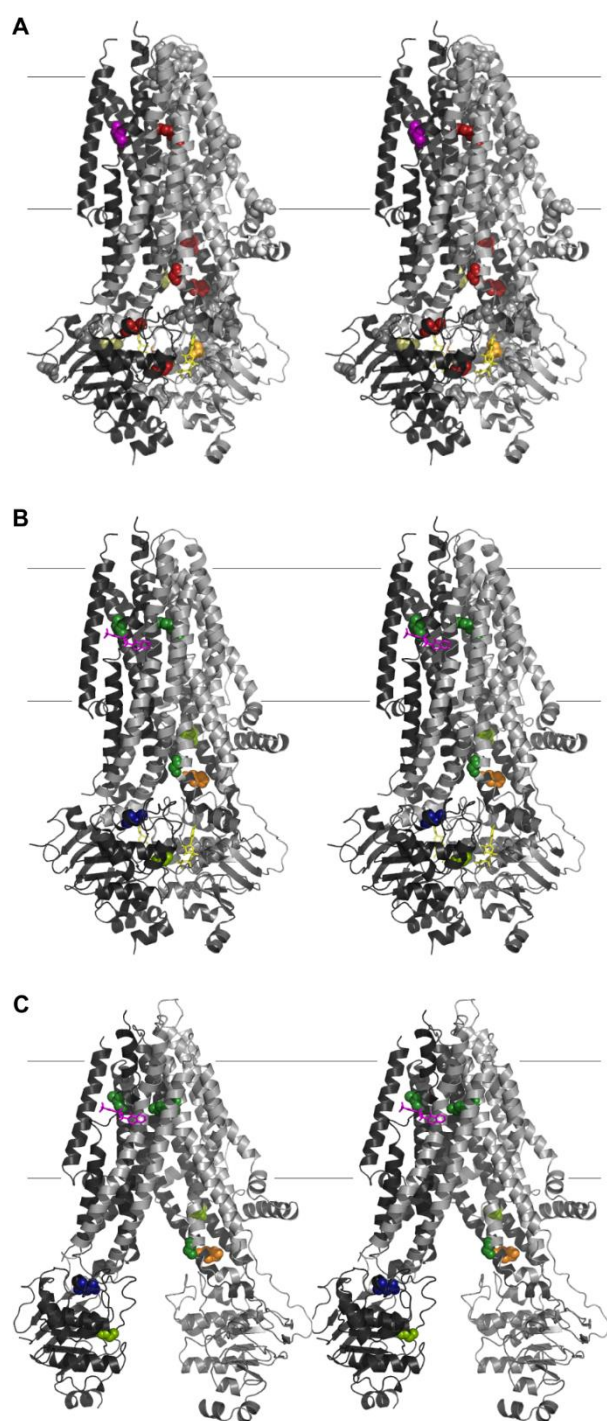
Mapping VX-770 sensitivity on cryo-EM structures. (**A**) Cartoon representation (cross-eye stereo) of phosphorylated, ATP-bound human CFTR, 6MSM (Zhang et al., 2018b), with sites of missense mutations in panel highlighted as spheres. Colours indicate degree of VX-770-potentiaton (fold potentiation, F < 5, grey; 5 < F < 10, white; 10 < F < 15, light yellow; 15 < F < 20, orange; 20 < F < 50, red; F > 50 purple). TMD1-NBD1 in light grey; TMD2-NBD2 in dark grey. Fine horizontal lines show approximate position of membrane boundary. (**B**) Only

939   positions with most efficacious VX-770 potentiation are shown. Magenta sticks show position

940   of bound VX-770 in 6O2P structure (Liu et al., 2019). Mutation-site residues are colour-coded

941   as in Fig. 4 (moving from cytosol to extracellular): G1349, light green; N1303, dark blue;

942   H1054, orange; G178, forest; H1085, light green; R347, forest right; L927 forest left. (**C**)

943   Orientation as in (**A,B**) but using atom coordinates of dephosphorylated human CFTR, 5UAK

944   (Liu et al., 2017).